





# Abundance stratification in Type Ia supernovae – VI. The peculiar slow decliner SN 1999aa

Charles J. Aouad<sup>1</sup>  <sup>1</sup>★, Paolo A. Mazzali,<sup>1,2</sup> Stephan Hachinger,<sup>3</sup> Jacob Teffs,<sup>1</sup> Elena Pian,<sup>4</sup> Chris Ashall<sup>5</sup> , Stefano Benetti<sup>6</sup> , Alexei V. Filippenko<sup>7</sup> and Masaomi Tanaka<sup>8,9</sup> 

<sup>1</sup>*Astrophysics Research Institute, Liverpool John Moores University, 146 Brownlow Hill, Liverpool L3 5RF, UK*

<sup>2</sup>*Max-Planck Institut für Astrophysik, Karl-Schwarzschild-Strasse 1, D-85748 Garching, Germany*

<sup>3</sup>*Leibniz Supercomputing Centre (LRZ) of the BAdW, Boltzmannstraße 1, D-85748 Garching, Germany*

<sup>4</sup>*INAF-IASF-Bo, via Gobetti, 101, I-40129 Bologna, Italy*

<sup>5</sup>*Institute for Astronomy, University of Hawai'i at Manoa, 2680 Woodlawn Dr, Hawai'i, HI 96822, USA*

<sup>6</sup>*INAF, Osservatorio Astronomico di Padova, Vicolo dell'Osservatorio 5, I-35122 Padova, Italy*

<sup>7</sup>*Department of Astronomy, University of California, Berkeley, CA 94720-3411, USA*

<sup>8</sup>*Astronomical Institute, Tohoku University, Aoba, Sendai 980-8578, Japan*

<sup>9</sup>*Division for the Establishment of Frontier Sciences, Organization for Advanced Studies, Tohoku University, Sendai 980-8577, Japan*

Accepted 2022 July 14. Received 2022 July 13; in original form 2022 April 3

## ABSTRACT

The abundance distribution in the ejecta of the peculiar slowly declining Type Ia supernova (SNe Ia) SN 1999aa is obtained by modelling a time series of optical spectra. Similar to SN 1991T, SN 1999aa was characterized by early-time spectra dominated by Fe III features and a weak Si II 6355 Å line, but it exhibited a high-velocity Ca II H&K line and morphed into a spectroscopically normal SN Ia earlier. Three explosion models are investigated, yielding comparable fits. The innermost layers are dominated by  $\sim 0.3 M_{\odot}$  of neutron-rich stable iron-group elements, mostly stable iron. Above that central region lies a  $^{56}\text{Ni}$ -dominated shell, extending to  $v \approx 11\,000\text{--}12\,000\text{ km s}^{-1}$ , with mass  $\sim 0.65 M_{\odot}$ . These inner layers are therefore similar to those of normal SNe Ia. However, the outer layers exhibit composition peculiarities similar to those of SN 1991T: The intermediate-mass elements shell is very thin, containing only  $\sim 0.2 M_{\odot}$ , and is sharply separated from an outer oxygen-dominated shell, which includes  $\sim 0.22 M_{\odot}$ . These results imply that burning suddenly stopped in SN 1999aa. This is a feature SN 1999aa shares with SN 1991T, and explains the peculiarities of both SNe, which are quite similar in nature apart from the different luminosities. The spectroscopic path from normal to SN 1991T-like SNe Ia cannot be explained solely by a temperature sequence. It also involves composition layering differences, suggesting variations in the progenitor density structure or in the explosion parameters.

**Key words:** line: identification – nuclear reactions, nucleosynthesis, abundances – radiative transfer – supernovae: general – supernovae: individual: SN 1999aa.

## 1 INTRODUCTION

Type Ia supernovae (SNe Ia) are among the most luminous transients in the Universe. They are thought to be the thermonuclear explosions of carbon–oxygen (CO) white dwarfs close to the Chandrasekhar limit (Hillebrandt & Niemeyer 2000; Mazzali et al. 2007; Livio & Mazzali 2018). A relation between the peak luminosity with the width of the light curve (Phillips 1993) makes SNe Ia standardizable candles and has led to their practical use as distance indicators and for the discovery of dark energy (Perlmutter et al. 1998; Riess et al. 1998).

The rise of the SNIa light curve is caused by the deposition of the gamma-rays and positrons emitted in the decay of the  $^{56}\text{Ni}$  synthesized during the explosion (Arnett 1982; Kuchner et al. 1994; Mazzali et al. 1998, 2001). The optical photons created in this process remain trapped until the ejecta become optically thin as they expand (Mazzali et al. 2001), allowing their diffusion. Therefore,

the peak of the light curve is directly proportional to the mass of  $^{56}\text{Ni}$  synthesized, while its width is related to the photon diffusion time, which is a function of ejected mass, kinetic energy, the radial distribution of  $^{56}\text{Ni}$ , and of the effective opacity, which is itself a function of temperature, density, and composition (Woosley et al. 2007).

Even though the majority of SNe Ia constitute a nearly equivalent group of intrinsically bright events and their spectroscopic features are fairly similar, observations indicate a scatter in their spectroscopic properties (Branch 2001; Silverman et al. 2012a; Jha, Maguire & Sullivan 2019; Siebert et al. 2019); see Filippenko (1997) for a review.

A question that arises is how distinct these events are. A clear separation could mean that they are of intrinsically different nature, while a continuity of properties would suggest quasi-similar events, with the observed diversity being caused by smoothly changing parameters. Important factors are the physical mechanism through which the white dwarf reaches ignition densities, the mass at explosion, and the explosion mechanism.

\* E-mail: [charlesaouad@asncid.ae](mailto:charlesaouad@asncid.ae); [C.J.Aouad@2020.ljmu.ac.uk](mailto:C.J.Aouad@2020.ljmu.ac.uk)

Different regimes under which the burning flame propagates lead to different nucleosynthetic yields, different composition structures, and therefore different spectral features. Simulations of pure deflagration models were unable to reproduce  $^{56}\text{Ni}$  masses of  $\sim 0.5 M_{\odot}$  and kinetic energies  $\sim 10^{51}$  erg, as derived from observations (Mazzali et al. 2007). In contrast, a pure detonation, in which the burning front propagates supersonically and ignites the fuel by compressive heating, incinerates the whole star to iron-group (hereafter, Fe-group) nuclei and cannot explain the presence of intermediate-mass elements (IMEs) in the ejecta outer layers. Alternative successful models have been proposed in which the deflagration front transits to a detonation at some specific density (deflagration to detonation transition, or DDT, Khokhlov 1991b). One-dimensional simulations of delayed-detonation models have proven successful in reproducing many of the observed spectral features of SNe Ia, in particular, the presence of a layer of IMEs, the product of partial burning of carbon and oxygen. These models can also account for the energy budget of the most energetic events and for the observed photospheric velocities. However, the exact physics of how this transition occurs is still a subject of extensive research (Woosley 2007).

The early-time spectra of normal SNe Ia are characterized by lines of singly ionized IMEs such as Mg, Si, S, Ca, and Fe-group elements. As time progresses, Fe lines increase in strength until they dominate the appearance of the spectrum a few weeks after maximum light (Filippenko 1997; Parrent, Friesen & Parthasarathy 2014). However, in some ‘peculiar’ events characterized by high luminosity (SN 1991T, and SNe of its subgroup; e.g. Filippenko et al. 1992), singly ionized IMEs only start to appear near maximum light, never reaching the same intensity as in normal SNe Ia. Their early-time spectra are instead dominated by doubly ionized species such as Fe III and Si III. The presence of these lines requires high temperatures in the outer ejecta.

SNe Ia with properties intermediate between those of SN 1991T and normal SNe Ia have been discovered. One case in particular is that of SN 1999aa, the subject of this study (Garavini et al. 2004; Jha et al. 2006; Matheson et al. 2008). Similar to SN 1991T, SN 1999aa was a slow decliner, with  $\Delta m_{15}(B)$  measurements ranging from 0.75 mag (Kriszian et al. 2000) to 0.85 mag (Jha et al. 2006). The earliest spectra of SN 1999aa resemble those of SN 1991T in being dominated by Fe III lines and by the weakness of singly ionized IME lines, in particular Si II 6355 Å. However, unlike SN 1991T, they showed a high-velocity Ca II H&K feature. SN 1999aa morphed to looking like a normal SNe Ia earlier than did SN 1991T. In fact, 1 week before  $B$  maximum, Si II 5468, 5654 Å and Si II 6355 Å were already visible in SN 1999aa. Figs 1 and 2 show optical spectra of SN 1999aa compared to SN 1991T and the spectroscopically normal SN 2003du, respectively  $\sim 10$  d before and near  $B$  maximum.

It has been suggested that SN 1999aa and similar SNe Ia [e.g. SNe 1998es (Ayani & Yamaoka 1998); 2012cg (Silverman et al. 2012c); and 1999dq, 2001eh, 2002hu, 2006cz, and 2008Z (Silverman, Kong & Filippenko 2012b)] constitute a subclass of their own. Silverman et al. (2012b) estimate the rate of SN 1999aa-like SNe Ia to be comparable to that of SN 1991T-like events.

A theoretical understanding of SN 1999aa should help clarify the spectroscopic sequence from normal to SN 1991T-like events. A first step toward this is to derive the composition and stratification of the ejecta. This can be done using the so-called abundance tomography technique (Stehle et al. 2005), which involves modelling a temporal series of spectra to reproduce their features consistently. At early times, the spectra are characterized by a pseudo-continuum on which P Cygni profiles of the lines that dominate near the momentary photosphere are superimposed. As the ejecta expand,

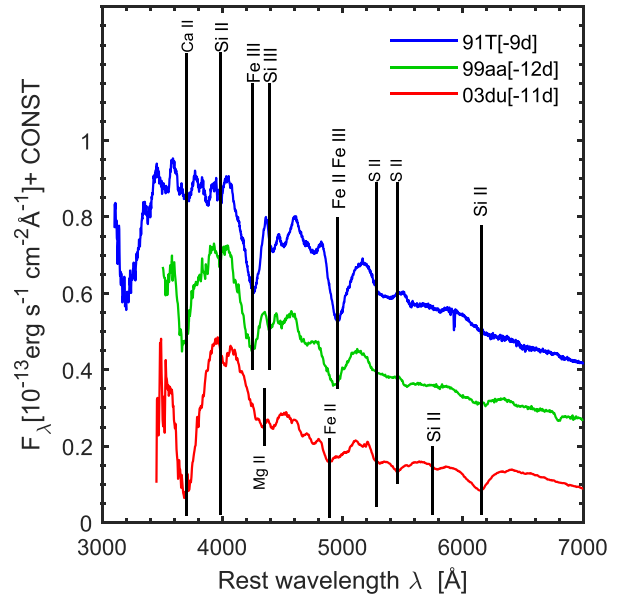


**Figure 1.** Early-time spectra of SN 1991T (top panel), SN 1999aa (middle panel), and the normal SN 2003du (bottom panel). Major absorption features are marked. Epochs are given in days relative to  $B$ -band maximum brightness.

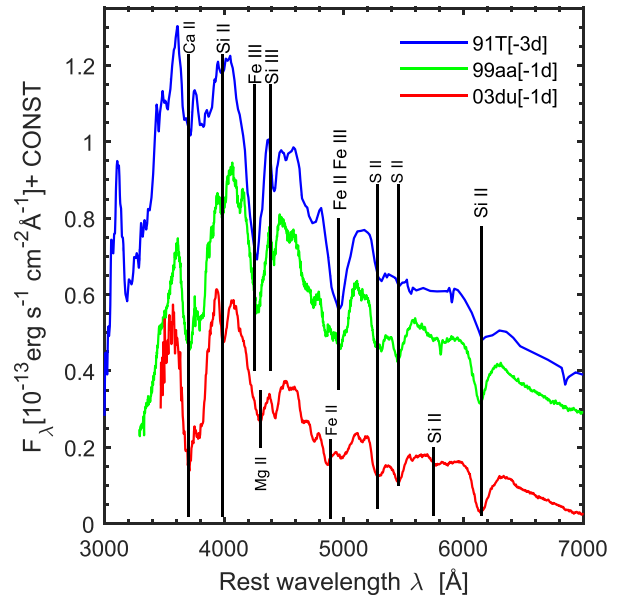


**Figure 2.** Same as Fig. 1, but for near-maximum-brightness spectra.

the photosphere recedes inward and reveals progressively deeper layers. This approach was successfully used to model several SNe Ia: SN 2002bo (Stehle et al. 2005), SN 2004eo (Mazzali et al. 2008), SN 2003du (Tanaka et al. 2011), SN 1991T (Saselli et al. 2014), and SN 1986G (Ashall et al. 2016).

Here, we use the abundance tomography technique to investigate the properties of SN 1999aa. In Section 2, we describe the data used, and in Section 3 we explain the modelling methods. We present our modelling results in Sections 4 and 5. In Section 6, we discuss the abundance tomography results. We use the derived abundances to compute a bolometric light curve in Section 7, and Section 8 discusses our results. Our conclusions are drawn in Section 9.

**Table 1.** Late-time photometry of SN 1999aa.

UT date	JD <sup>a</sup>	Epoch <sup>b</sup> (d)	$U$ (1 $\sigma$ ) (mag)	$B$ (1 $\sigma$ ) (mag)	$V$ (1 $\sigma$ ) (mag)	$R$ (1 $\sigma$ ) (mag)	$I$ (1 $\sigma$ ) (mag)
03/11/1999 <sup>c</sup>	485.170	+248.9	22.202 (0.086)	20.987 (0.075)	20.811 (0.045)	22.019 (0.127)	–
11/12/1999 <sup>c</sup>	523.170	+286.4	–	21.381 (0.044)	21.192 (0.029)	22.705 (0.079)	–
14/12/1999 <sup>c</sup>	526.098	+289.2	23.067 (0.067)	21.486 (0.025)	21.189 (0.026)	22.769 (0.099)	21.494 (0.071)
05/01/2000 <sup>c</sup>	548.086	+310.9	23.414 (0.079)	21.844 (0.028)	21.522 (0.027)	23.059 (0.050)	22.112 (0.094)

Note.

<sup>a</sup>JD–2 451 000.

<sup>b</sup>Rest-frame time, since  $B$  maximum.

<sup>c</sup>Instrument: *TNG* + *OIG*.

**Table 2.** Spectra of SN 1999aa and modelling parameters.

UT date 1999	JD <sup>a</sup>	Epoch <sup>b</sup> (d)	Telescope/ instrument	log $L$ ( $L_{\odot}$ )	$v$ (km s <sup>–1</sup> )	$T$ (rad) (K)
12/02 <sup>c</sup>	221.5	–11.0	Lick 3 m/Kast	9.220	12 600	12 310
13/02 <sup>d</sup>	222.5	–10.0	NOT	9.315	12 300	12 735
			2.6 m/ALFOSC			
14/02 <sup>e</sup>	223.83	–8.8	FLW 1.5 m/FAST	9.440	12 000	12 946
15/02 <sup>e</sup>	224.78	–7.8	FLW 1.5 m/FAST	9.470	11 500	13 335
16/02 <sup>e</sup>	225.74	–6.9	FLW 1.5 m/FAST	9.510	11 200	13 440
17/02 <sup>d</sup>	226.5	–6.1	APO 3.5 m/DIS	9.530	10 950	13 378
18/02 <sup>e</sup>	227.75	–4.9	FLW 1.5 m/FAST	9.590	10 550	13 695
19/02 <sup>e</sup>	228.78	–3.8	FLW 1.5 m/FAST	9.610	10 300	13 490
20/02 <sup>e</sup>	229.79	–2.9	FLW 1.5 m/FAST	9.610	10 000	13 239
21/02 <sup>e</sup>	230.79	–1.9	FLW 1.5 m/FAST	9.595	9600	13 029
23/02 <sup>c</sup>	232.5	–0.2	Lick 3 m/Kast	9.590	9300	12 296
25/02 <sup>d</sup>	234.5	+1.8	Lick 3 m/Kast	9.560	8900	11 380
03/03 <sup>d</sup>	240.5	+7.7	MDM 2.4 m/Mk III	9.310	7150	12 778
09/03 <sup>c</sup>	246.5	+13.6	Keck-I/LRIS	9.170	5500	11 663
12/03 <sup>c</sup>	249.5	+16.6	Lick 3 m/Kast	9.130	4250	11 162

Note. <sup>a</sup> JD–2 451 000.

<sup>b</sup> Rest-frame time, since  $B$  maximum.

<sup>c</sup> Silverman et al. (2012a).

<sup>d</sup> Garavini et al. (2004).

<sup>e</sup> Matheson et al. (2008).

## 2 DATA

SN 1999aa was discovered independently by Nakano, Kushida & Kushida (1999), Armstrong & Schwartz (1999), and Qiao et al. (1999). The host galaxy is NGC 2595, a barred spiral of morphological classification SAB(rs)c with redshift  $z = 0.0144$  (Epinat et al. 2008; van Driel et al. 2016). Distance moduli to the galaxy based on the Tully–Fisher relation range from  $\mu = 32.30 \pm 0.53$  mag (Bottinelli et al. 1985) to  $\mu = 34.44 \pm 0.47$  mag (Theureau et al. 2007). Distances using the light curve of SN 1999aa vary from  $\mu = 33.43 \pm 0.16$  mag (Amanullah et al. 2010) to  $\mu = 34.58 \pm 0.24$  mag (Riess et al. 2004).

Photometric data are taken from Jha et al. (2006), Krisciunas et al. (2000), Qiao et al. (1999), Armstrong & Schwartz (1999), Yoshida et al. (1999), and Altavilla et al. (2004). Late-time unpublished data are based on observations collected with the Optical Imager Galileo (OIG) at *Telescopio Nazionale Galileo* (*TNG*) – La Palma. The *TNG* + *OIG* *UBVRI* frames were reduced following standard procedures and made use of the ECSNOOPY package (Cappellaro 2014) using the point spread function fitting technique for the SN measurement. The *BVRI* SN magnitudes were then calibrated with reference to the magnitudes of field stars retrieved from Krisciunas et al. (2000), while for the  $U$  band, we converted the SDSS catalogue magnitudes

of the local sequence into Johnson  $U$  following Chonis & Gaskell (2008). The final *TNG* + *OIG* magnitudes are shown in Table 1, where the mean photometric errors, estimated with artificial-star experiments, are given in parentheses.

The spectra used in this study are available at the Weizmann Interactive Supernova Data Repository (Yaron & Gal-Yam 2012); they are listed in Table 2. The spectra were calibrated against photometric observations. Calibration was performed in the  $U$ ,  $B$ ,  $V$ , and  $R$  bands by multiplying the spectra with a line of constant gradient or with a low-order smoothed spline. We ensured that the flux in the spectra in any passband did not vary by more than  $\sim 10$  per cent from the observed flux in that filter passband.

## 3 MODELLING TECHNIQUES

Spectra in the photospheric phase have been modelled using a Monte Carlo spectrum synthesis code (Mazzali & Lucy 1993; Lucy 1999a,b). The code assumes a sharp photosphere. As the ejecta expand homologously, the photosphere recedes in velocity space and consequently in mass coordinate. Thermal equilibrium is assumed. Photons emitted from the photosphere propagate through the expanding ejecta and interact with the gas through line absorption, including line branching (Mazzali 2000), or electron scattering. The required input parameters are the density structure of the SN ejecta, the emergent bolometric luminosity  $L_{\text{Bol}}$ , the photospheric velocity  $v_{\text{ph}}$ , the time from the explosion  $t_0$ , and the abundances of the elements as a function of depth above the photosphere.

The distance and the extinction to the SN are needed in order to scale the flux. Since the distance to NGC 2595 is not known accurately, we treat it as a free parameter, within the range allowed by the literature. We tested several values of the distance modulus ( $\mu$ ) for three different spectra. For larger distances the high luminosity causes a high temperature, which in turn leads to unrealistic ionization. The opposite happens for distances that are too small. The best models are obtained with  $\mu = 34.00$  mag, which is very close to the mean value calculated using the various distance moduli reported in the literature,  $\bar{\mu} = 33.975 \pm 0.34$  mag. We adopt an extinction value  $E(B - V) = 0.04$  mag (Schlegel, Finkbeiner & Davis 1998) for the Milky Way and assume  $E(B - V) = 0.00$  mag for the host galaxy (Krisciunas et al. 2000). We also tested different rise times, between 19 and 21 d; the best results are obtained with a value of 20 d.

We use three different density–velocity distributions: the classical fast deflagration model, W7 (Nomoto et al. 1984), and two more energetic delayed-detonation models, DD2 and DD3 from Iwamoto et al. (1999). These density profiles are shown in Fig. 3.

Having fixed  $\mu$ ,  $t_0$ , and  $E(B - V)$ , the modelling starts with the earliest spectrum. Different values of  $L_{\text{Bol}}$  are tried until the synthetic spectrum matches the observed one in flux. After that,  $v_{\text{ph}}$  is iterated to match the position of the spectral features and the overall

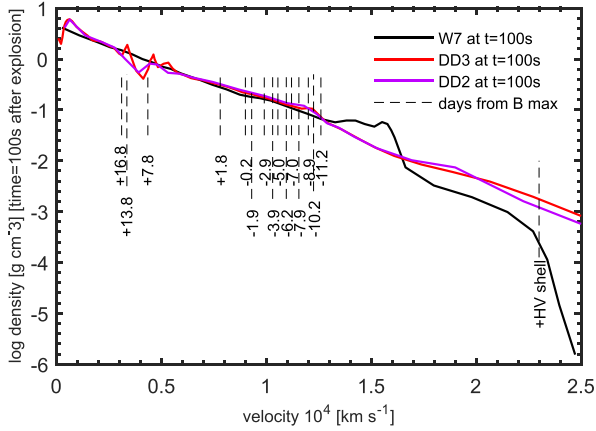


**Figure 3.** The three density profiles used in the modelling: W7 (Nomoto, Thielemann & Yokoi 1984), DD2, and DD3 (Iwamoto et al. 1999). Vertical dashed lines mark the photospheres of the synthetic spectra.

temperature. In parallel, the abundances are modified until the model matches the observation.

For the following spectrum in the sequence, a new, smaller  $v_{\text{ph}}$  is defined. This will introduce a new shell where new abundances can be determined. This process is repeated for each spectrum. As the spectra evolve, deeper layers are revealed and the abundance stratification is gradually built.

#### 4 THE PHOTOSPHERIC PHASE

We modelled 15 spectra, from day  $-11$  to day  $+14$  from  $B$  maximum. The input parameters are shown in Table 2. The synthetic spectra corresponding to the three explosion models we use are shown in Figs 4, 8, 9, 10, and 11, overlaid on the observed spectra.

##### 4.1 The early-time spectra

In Fig. 4, we show models for the earliest spectra, ranging from  $-11$  to  $-9$  d from  $B$  maximum. The synthetic spectra reproduce the observed features well. In particular, they exhibit deep absorption lines of Fe III and Si III, and the overall flux matches the observed flux, except in the redder bands. The velocity of the photosphere starts at  $12\,600\text{ km s}^{-1}$  and decreases to  $12\,000\text{ km s}^{-1}$ .

###### 4.1.1 Fe-group elements

A small amount of iron is needed at the outer shells to reproduce the deep observed features near  $4250$  and  $5000\text{ Å}$ . This is stable Fe; at these early stages,  $^{56}\text{Ni}$  would not have had time to decay significantly into  $^{56}\text{Fe}$ . The mass fraction of Fe at  $v > 12\,600\text{ km s}^{-1}$  needed to reproduce the observed features is  $\sim 0.015\text{--}0.018$  (Fig. 5). The presence of stable Fe in the outer shells has been reported in other SNe Ia. Sasdelli et al. (2014) give a solar abundance [ $X(\text{Fe}_{\odot}) = 0.001$ , Asplund et al. (2009)] for SN 1991T, while Tanaka et al. (2011) report values of  $\sim 0.003\text{--}0.005$  for SN 2003du. Our values are significantly supersolar.

Small amounts of  $^{56}\text{Ni}$ , Ti, and Cr are needed at these epochs to block the ultraviolet (UV) flux and redistribute it redward. The abundance of  $^{56}\text{Ni}$  is not constrained at these epochs, as no visible line in the spectrum is reproduced by  $^{56}\text{Ni}$  or Co alone. Unfortunately, the spectra of SN 1999aa do not extend bluer than  $\sim 3400\text{ Å}$ , where a

prominent feature dominated by Co III should be expected at  $\sim 3200\text{ Å}$  (Mazzali, Danziger & Turatto 1995; Stehle et al. 2005; Sasdelli et al. 2014).

###### 4.1.2 Calcium

The early-time spectra of SN 1999aa show a deep absorption line near  $3700\text{ Å}$ , with strength intermediate between that of normal SNe Ia and SN 1991T (Garavini et al. 2004). This feature is due to high-velocity Ca II H&K (Mazzali et al. 2005b).

We are able to produce it with  $X(\text{Ca}) \approx 0.0035$  at  $v > 21\,000\text{ km s}^{-1}$  with the W7 model. The DD2 and DD3 models have more mass at high velocity, and therefore  $X(\text{Ca}) \approx 0.00025$  is sufficient (see Tanaka et al. 2011). This is much less than the Ca abundance reported in some spectroscopically normal SNe Ia (Tanaka et al. 2008). However, those SNe exhibit a much stronger Ca II H&K lines and a much earlier appearance of the Ca II near-infrared (NIR) feature than in both SN 1999aa and SN 1991T. On the other hand, the abundance we obtained is similar to that obtained for SN 1991T, for which Sasdelli et al. (2014) estimate a Ca abundance  $< 0.0003$  at  $v > 17\,000\text{ km s}^{-1}$  using the DD3 density profile. Regardless of the density profile used, our results suggest that the abundance of Ca at high velocities is supersolar [ $X(\text{Ca}_{\odot}) = 0.00006$ , Asplund et al. (2009)].

The strength of the Ca II H&K feature is very sensitive not only to the Ca abundance at high velocity, but also to the parameters that directly affect ionization, in particular the electron density. The presence of free electrons decreases the ionization and favours singly ionized species (Mazzali et al. 2005a,b). Adding H results in a higher electron density. Following Tanaka et al. (2011), in Fig. 6 we show how the Ca II H&K feature can be reproduced with different Ca abundances coupled with different amounts of H at the outermost shells ( $v > 21\,000\text{ km s}^{-1}$ ). However, because of the degeneracy between the Ca abundance and the electron density, it is not possible to determine the Ca mass fraction. Hydrogen may result from the interaction of the ejecta with the circumstellar medium (Mazzali et al. 2005b) or may be a remnant of accretion on the surface of the WD (Livio & Mazzali 2018). Even though small amounts of H are sufficient to reduce the ionization at the dilute outermost layers, and therefore create the high-velocity features (HVs) ubiquitously observed in SNe Ia spectra (Mazzali et al. 2005b), larger amounts [ $X(\text{H}) \gtrsim 0.3$ ], will give rise to an H $\alpha$  feature that is not seen in the observed spectrum. The lack of H signatures can be taken as an argument against the single degenerate scenario (Marietta, Burrows & Fryxell 2000; Panagia et al. 2006) but it is not enough to rule it out (Justham 2011; Hachisu et al. 2012). For a review, see Livio & Mazzali (2018).

###### 4.1.3 Silicon, sulphur, and magnesium

The Si II 6355  $\text{Å}$  line is much weaker in the earliest spectra of SN 1999aa than in normal SNe Ia. It grows in strength as the spectra evolve. However, the feature near  $4400\text{ Å}$ , which is due to Si III 4553, 4568, 4575  $\text{Å}$ , is prominent in the earliest spectra, as the high temperature favours doubly ionized species. These Si lines are well reproduced in the synthetic spectra. The Si mass fraction is  $0.025$  at  $v > 12\,600\text{ km s}^{-1}$ , but it rapidly increases to  $0.73$  at  $v > 12\,300\text{ km s}^{-1}$ .

The two Si II features at  $5468$  and  $5654\text{ Å}$  are not present at these early epochs, and only start to show at day  $\sim -6$ . The Mg II 4481  $\text{Å}$  line is never visible in the spectra of SN 1999aa, as that region is dominated by Fe III lines.





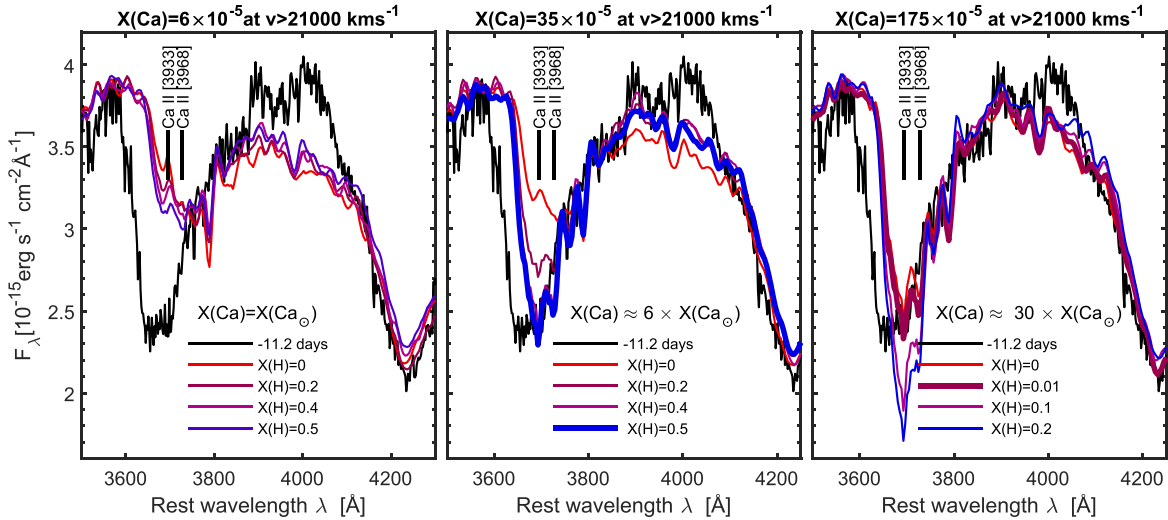


**Figure 6.** A close-up view of the Ca II H&K region, showing the observed spectrum at day  $-11$  compared to models computed with the W7 density profile using different abundances of Ca coupled with various amounts of H in the outermost shells.

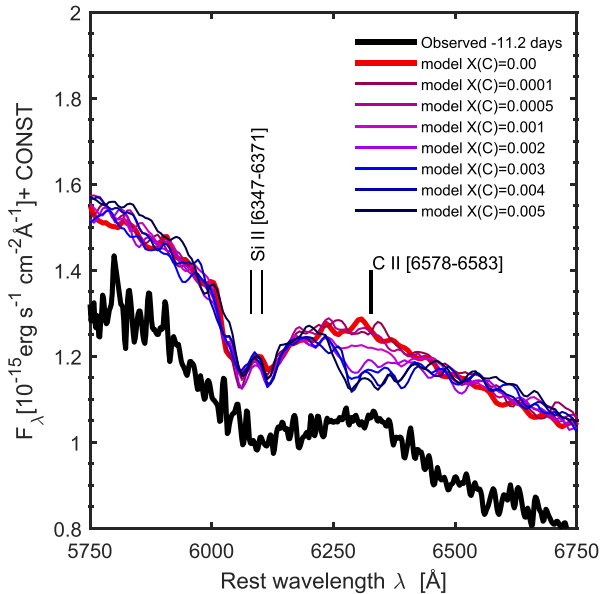


**Figure 7.** A close-up view of the spectrum showing the Si II–C II region. Small amounts of carbon can create an absorption line redward of the Si II line. A prominent C line is not seen in the observed spectrum.

contrast, Tanaka et al. (2011) report the presence of oxygen down to a velocity of  $9400 \text{ km s}^{-1}$  for the normal SN Ia 2003du.

## 4.2 Pre-maximum-light spectra

Figs 8 and 9 show spectra ranging from  $-8$  to  $-3$  d from  $B$  maximum. The photospheric velocity evolves from  $11\,500$  to  $10\,000 \text{ km s}^{-1}$ .

### 4.2.1 Fe-group elements

The Fe III lines observed near  $4300$  and  $5000 \text{ Å}$  increase in strength. Our synthetic spectra reproduce their evolution. At these epochs, the fraction of Fe originating from  $^{56}\text{Ni}$  decay becomes significant. At

day  $-7$ , it already constitutes 20 per cent of the total Fe mass fraction, increasing to 30 per cent at day  $-3$ . We obtain good fits for  $X(\text{Fe}_{\text{stable}}) \approx 0.1$  in the shells that are probed. The abundance of  $^{56}\text{Ni}$  increases from 0.05 at  $v = 11\,500 \text{ km s}^{-1}$  to 0.53 at  $v = 10\,950 \text{ km s}^{-1}$ .

### 4.2.2 Calcium

The synthetic spectra reproduce well the Ca II H&K feature. The Ca II NIR triplet is still not seen in the observed spectra at day  $-6$ , and this is confirmed in our synthetic spectra. The near-photospheric Ca abundance at these epochs is  $\sim 0.0015$  for all models.

### 4.2.3 Silicon and sulphur

The Si II  $6355 \text{ Å}$  line gets deeper with time. This is well replicated in our synthetic spectra, as are the Si III feature near  $4400 \text{ Å}$  and the Si II  $4130 \text{ Å}$  line. The Si abundance is 0.72 at  $v \approx 11\,500 \text{ km s}^{-1}$ , and it decreases to 0.26 at  $v \approx 10\,000 \text{ km s}^{-1}$ . The two Si II lines at  $5468$  and  $5654 \text{ Å}$  start to show at day  $-6$  and grow stronger with time. The sulphur abundance is 0.15 at  $v \approx 11\,500 \text{ km s}^{-1}$ , decreasing slightly to lower velocities.

### 4.2.4 Carbon and oxygen

C and O are not needed at these epochs. Any abundance of C would produce a line that is not seen in the observed spectra. Oxygen is not needed because the Fe-group elements and IMEs are sufficient to complete the composition at these velocities.

## 4.3 Spectra at maximum brightness

Fig. 10 shows spectra ranging from  $-2$  to  $+2$  d from  $B$  maximum. The photospheric velocity evolves from  $9600$  to  $8900 \text{ km s}^{-1}$ . The synthetic spectra predict excess flux redward of  $\sim 6000 \text{ Å}$ . At these epochs, as the photosphere recedes inside the  $^{56}\text{Ni}$ -dominated shell, energy is partially deposited above the photosphere, and the assumption of blackbody emission at the photosphere is not entirely correct.

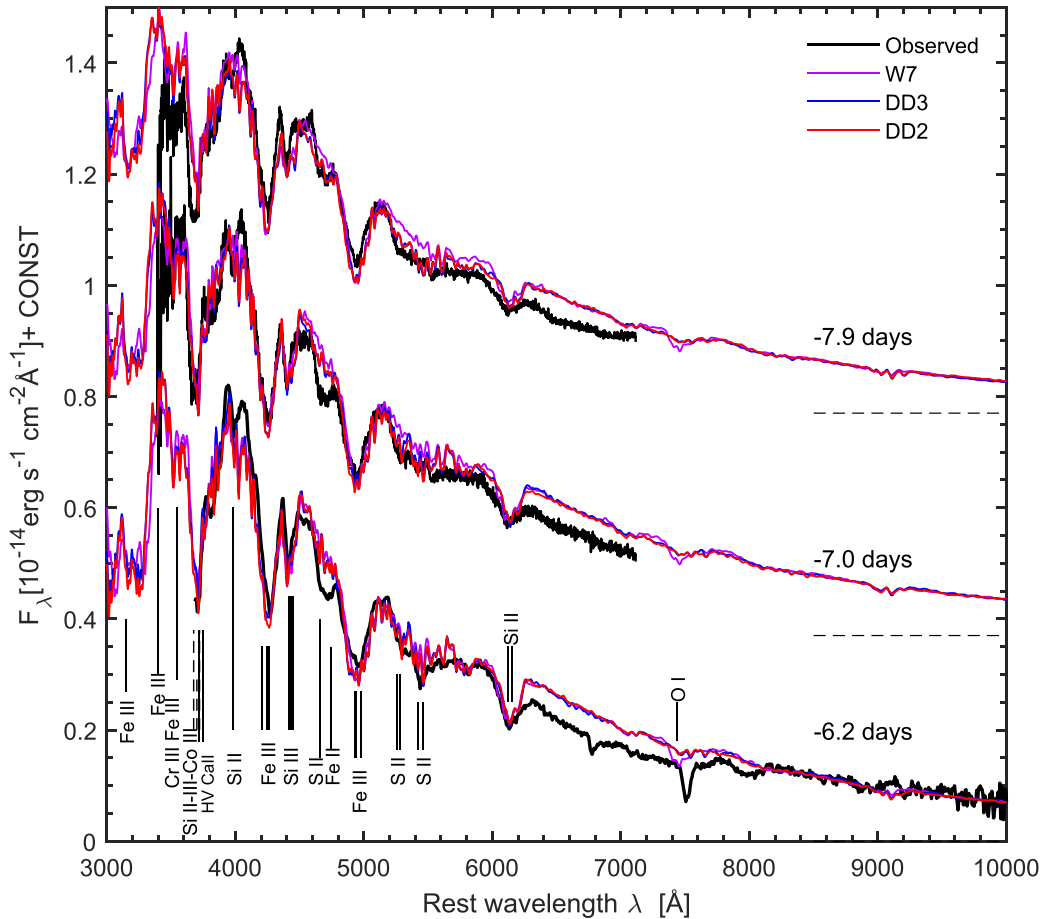


**Figure 8.** Spectra 1 week before  $B$ -band maximum. Epochs are shown with reference to  $B$  maximum. Features in the  $-6.2$  d spectrum near  $6780$  Å (weak) and  $7500$  Å are telluric. The spectra have been shifted in flux by a constant value. The horizontal dashed line marks the zero flux for each epoch.

#### 4.3.1 Fe-group elements

At these epochs, Fe lines are quite deep. The Fe abundance is high, because iron from  $^{56}\text{Ni}$  decay is now a significant contribution ( $\sim 30$  per cent) to the Fe abundance. The feature observed near  $4300$  Å is still dominated by Fe III. The Fe III feature near  $5000$  Å becomes broader because of the contribution of Fe II lines. This is reproduced reasonably well in our synthetic spectra.

#### 4.3.2 Calcium

The synthetic spectra still reproduce well both the depth and the shape of the Ca II H&K feature. At these epochs, it becomes contaminated by Si II and Co III lines in its bluer part and by Si II and Fe III lines in its redder part (see Silverman et al. 2015). The Ca II NIR triplet begins to appear 2 d after  $B$  maximum, and this is reproduced in the synthetic spectra. This feature is seen much earlier in spectroscopically normal SNe Ia, where it is much stronger than in SN 1999aa even  $\sim 12$  d before maximum light (Stehle et al. 2005; Mazzali et al. 2008; Tanaka et al. 2011). Instead, in SNe 1991T and 1999aa it only appears a few days after  $B$  maximum. Calcium extends down to  $v \approx 9600$  km s $^{-1}$ .

#### 4.3.3 Silicon and sulphur

The shape and depth of the prominent Si II  $6355$  Å line are well replicated in the synthetic spectra. The silicon abundance

is  $0.25$  at  $v \approx 9600$  km s $^{-1}$ , decreasing to  $0.1$  at  $v \approx 8900$  km s $^{-1}$ . Si II  $5468$ ,  $5654$  Å are now prominent, and increase in strength with time. Our synthetic spectra reproduce their evolution and the ratio of their depths reasonably well. The S abundance is  $0.12$  by mass at  $v \approx 9600$  km s $^{-1}$ , decreasing to  $0.05$  at  $v \approx 8900$  km s $^{-1}$ .

### 4.4 Post-maximum-light spectra

Fig. 11 shows spectra ranging from 8 to 17 d after  $B$  maximum. The photospheric velocity evolves from  $7150$  to  $4250$  km s $^{-1}$ . At these epochs, the quality of the fits starts degrading, as the photosphere resides deep in the  $^{56}\text{Ni}$ -dominated region. Therefore, we do not use these epochs to infer abundances, but rather employ the nebular-phase models. Nevertheless, the synthetic spectra reproduce the observed ones sufficiently well.

#### 4.4.1 Fe-group elements

At these epochs ( $\sim 30$ – $40$  d after the explosion), more than about 70 per cent of all Fe originates from the decay of  $^{56}\text{Ni}$ . The Fe II feature near  $5000$  Å splits into three components that are fairly reproduced in the synthetic spectra. This is the consequence of the lower degree of line blending at slower velocities.





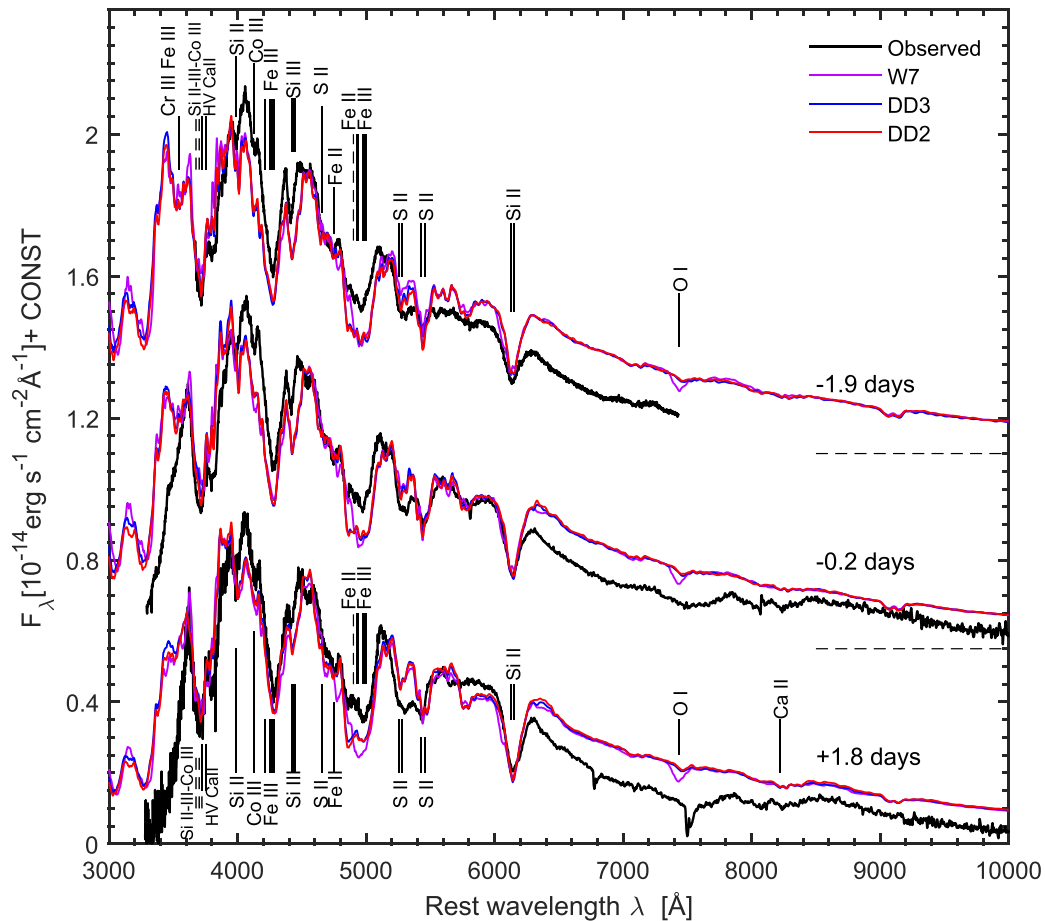


**Figure 10.** Near-maximum-light spectra. Epochs are shown with reference to  $B$  maximum. Features in the +1.8 d spectrum near 6780 Å (weak) and 7500 Å are telluric. The spectra have been shifted in flux by a constant value. The horizontal dashed line marks the zero flux for each epoch.

for the outer regions derived from the early-time models, we now modify the abundances in the inner layers ( $v < 8000 \text{ km s}^{-1}$ ) in order to optimize the fits. A best fit is defined empirically, as it is impossible to match every line and not all lines carry the same weight of information, but basically we need to match both the intensity of the lines (which depends on the amount of  $^{56}\text{Ni}$  as well as of the emitting element) and their width (which traces the radial distribution of the emitting elements as well as indirectly that of  $^{56}\text{Ni}$ , since heating from radioactive decay must reach the emitting region). Collisional data are not perfectly known for many of the Fe lines in the optical region, so we cannot expect that all emission lines will be simultaneously reproduced. We focus therefore on reproducing the strongest emission lines. Fortunately, these include emission from both Fe III (the emission near 4800 Å) and Fe II (the emission near 5200 Å), so we can control the ionization of Fe, which is the dominant species in the inner ejecta at the time of the nebular spectra.

Figs 12 and 13 show the fits to the two nebular spectra. We used the same composition at both epochs, which confirms that radioactive decay is the sole powering mechanism of the SN luminosity.

The mass of  $^{56}\text{Ni}$  synthesized is  $\sim 0.65 M_{\odot}$  for all three models. The stable Fe mass is highest when using DD2, but it is still within the expected range of values (Mazzali et al. 2001). The extra Fe seems to be located at 9000–12 000  $\text{km s}^{-1}$ . Stable Fe is necessary to reduce the ionization degree and obtain a reasonable ratio of the [Fe III] and [Fe II]-dominated features. The mass of stable Ni is quite

low, and this is reflected by the weakness of the only visible Ni line, [Ni II] 7380 Å. This is common to all SNe Ia we have studied, and suggests that little stable Ni is synthesized even in the dense innermost regions of SNe Ia. A moderate degree of clumping is used (filling factor  $\geq 0.5$ ) in the  $^{56}\text{Ni}$ -dominated regions. Further clumping may lead to a drop in ionization at later times, as seen in SN 2011fe (Graham et al. 2015) and SN 2014J (Mazzali et al. 2020), but the available spectra of SN 1999aa are too early and too close in time to show any change. The combined early-time and late-time studies complete the abundance tomography experiment. The main elements in the ejecta are summarized in Table 3, where the expected  $E_K$  is also shown and compared to that of the original models.

## 6 ABUNDANCE TOMOGRAPHY

The mass fractions of different elements as a function of mass and velocity for the three density profiles are shown in Figs 14, 15, and 16, compared to the original abundance distributions in the hydrodynamical models (Nomoto et al. 1984; Iwamoto et al. 1999).

The inner core, up to  $v \approx 2500 \text{ km s}^{-1}$ , is dominated by stable Fe with a small amount of  $^{56}\text{Ni}$ . Stable Fe-group elements are synthesized by electron capture in the high-density/-temperature core ( $\rho \geq 10^8 \text{ g cm}^{-3}$ ;  $T \geq 5 \times 10^9 \text{ K}$ ) during the explosion, when nuclear statistical equilibrium is attained (Arnett 1982; Iwamoto et al. 1999;

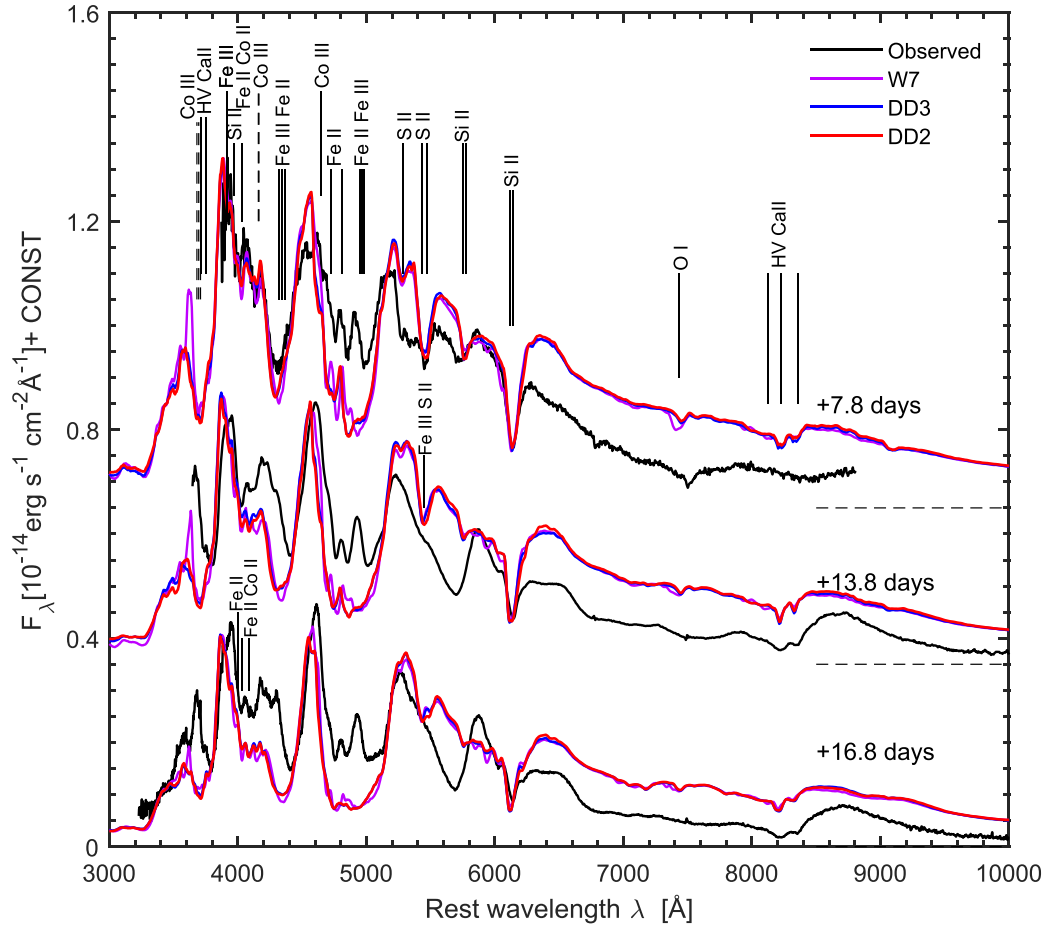


**Figure 11.** Post-maximum-light spectra. Epochs are shown with reference to *B* maximum. Features in the +7.8 d spectrum near 6780 Å (very weak) and 7500 Å (weak) are telluric. The spectra have been shifted in flux by a constant value. The horizontal dashed line marks the zero flux for each epoch.

Woosley et al. 2007). The distribution of these elements that we derive is in general agreement with the various explosion models.

Moving outward, a  $^{56}\text{Ni}$ -dominated shell extends over  $\sim 0.8\text{--}1\text{ M}_{\odot}$ , out to  $v \approx 11\,000\text{ km s}^{-1}$ . Practically no stable Ni is present in this region, in contrast to all explosion models, while a significant amount of stable iron is present, similar to the model prediction in the inner regions of this shell but significantly above it in regions between  $3000\text{ and }8000\text{--}9000\text{ km s}^{-1}$ . This results in a larger production of stable Fe, at the expense of stable Ni, when our results are compared to the original models.

A narrow, IME-dominated shell characterizes velocities  $\sim 11\,000\text{--}12\,000\text{ km s}^{-1}$ . The abundance of IMEs decreases sharply above this velocity. In the hydrodynamic models, this shell extends to higher velocities. The confinement of the IMEs in a narrow shell was also suggested by Garavini et al. (2004) based on the velocity evolution of Si II 6355 Å. IMEs are the result of incomplete burning, when the densities drop to  $\sim 10^7\text{ g cm}^{-3}$ . Their sudden depletion suggests a sudden drop in burning, which may be a key element to understand the structure of the progenitor and the explosion mechanism. The weakness of the IME lines in the early-time spectra of SN 1999aa and other SN 1991T-like SNe Ia is therefore an abundance effect (see Filippenko et al. 1992; Jeffery et al. 1992), and not only a temperature effect. The abundance of  $^{56}\text{Ni}$  is still significant in this region.

Above the IME shell, an O-rich outer layer is present. We could not conclusively determine the C abundance as no strong C features

are observed. These outermost layers determine the appearance of the earliest spectra (see Fig. 3). Small amounts of Ca are necessary to form the Ca II H&K lines. A small abundance of stable Fe, roughly a few per cent, is necessary in order to form Fe lines at the earliest epochs. This is larger than the solar abundance.

The host-galaxy metallicity at the location of SN 1999aa is  $12 + \log(\text{O}/\text{H}) = 8.45$  (Galbany et al. 2016), about a factor of two below solar, suggesting that Fe at these shells is probably the result of explosive nucleosynthesis (see also Hachinger et al. 2013). In general, the presence of Fe at these shells is more consistent with DD2 and DD3 than with W7. Only a very small amount of  $^{56}\text{Ni}$  is present in the O-rich layer, as also previously reported in other SNe Ia (Stehle et al. 2005; Tanaka et al. 2011). The distribution of  $^{56}\text{Ni}$  is in general consistent with the explosion models.

## 7 LIGHT CURVE

### 7.1 Building the bolometric light curve

We constructed a bolometric light curve of SN 1999aa in the range of  $3000\text{--}10\,000\text{ Å}$ . The *UBVR* light curves were splined with a time resolution of 1 d, dereddened with the extinction curve of Cardelli, Clayton & Mathis (1989) using  $E(B - V) = 0.04\text{ mag}$  (Schlegel et al. 1998) and reduced to the rest frame. Daily spectral energy distributions in the above wavelength interval were constructed using

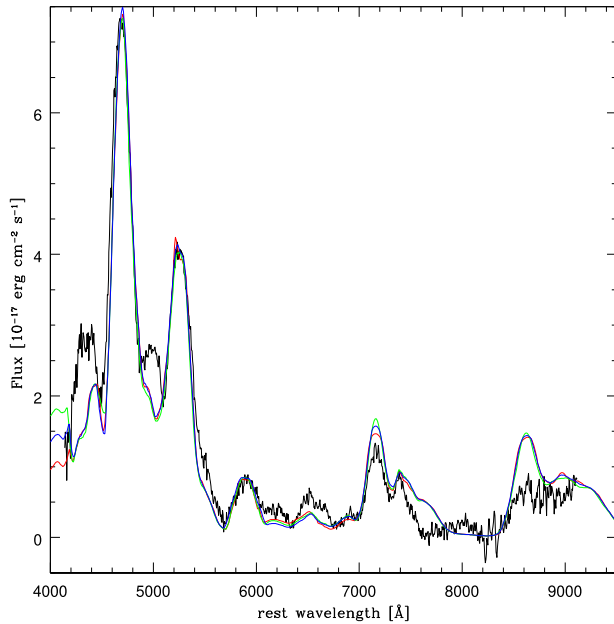


**Figure 12.** Nebular-phase spectrum obtained on 1999 November 9, corresponding to 255 rest-frame days after *B* maximum brightness (black). The emissions near 5200 and 7200 Å are dominated by [Fe II] lines, while the emission near 4700 Å is dominated by [Fe III] lines. A Na I D-dominated emission line is visible near 5900 Å, while [Ni II] 7380 is responsible for a weak emission line. The blue, green, and red curves are the synthetic spectra obtained with DD3, DD2, and W7, respectively.

the flux zero-points of Fukugita, Shimasaku & Ichikawa (1995). For each epoch, we integrated the *U* – to *I*-band flux after interpolating the flux between the central wavelengths of the filters, and added at the blue and red boundaries of the interval the fluxes obtained extrapolating the spectrum with a flat power law to 3000 and 10 000 Å, respectively. The final bolometric light curve was resampled to the epochs of the actual optical observations. Since the first four measurements (i.e. prior to 1999 February 13.5) are unfiltered, they have been assimilated to *V*-band fluxes and a bolometric correction was applied to them equivalent to the difference between the early bolometric magnitude and the simultaneous *V*-band magnitude. Bolometric luminosities were obtained using the luminosity distance of NGC 2595 (63.1 Mpc); they are shown in Fig. 17 as black circles.

We evaluated the contribution of the NIR flux to the bolometric light curve. NIR photometry in the *J* and *K* bands is available at four epochs after maximum brightness (Krisciunas et al. 2000). The NIR luminosity in the range of 10 000–24 000 Å was constructed following a procedure analogous to the one adopted in the optical. Flat power laws were used to estimate the flux shortward of the *J* band and longward of the *K* band. Luminosities over the range 3000–24 000 Å at the four epochs when NIR observations are available are shown in Fig. 17 as red circles.

No UV observations are available for SN 1999aa, so we cannot account for flux at wavelengths shorter than the Bessell *U* filter ( $\lambda < 3000$  Å). The UV should make a significant contribution only at the earliest epochs (see below).

## 7.2 Modelling the bolometric light curve

Having studied the abundance distribution for a few possible explosion models in SN 1999aa, one way to verify the results is to test them

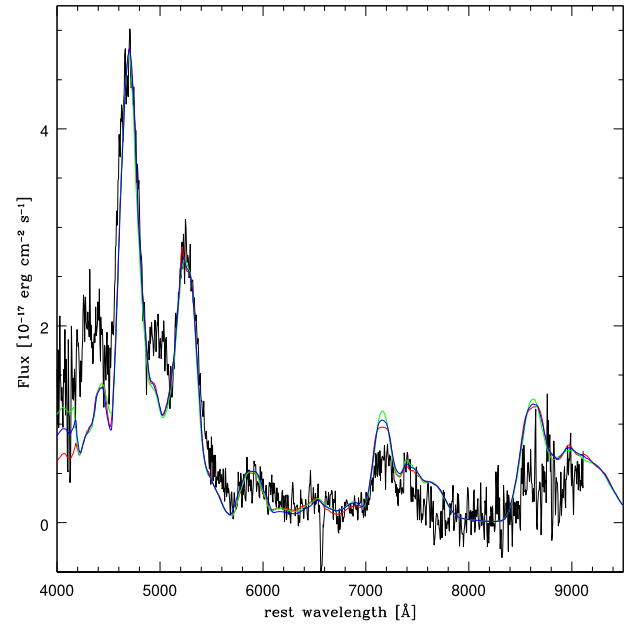


**Figure 13.** Nebular-phase spectra obtained on 1999 December 5, corresponding to 281 rest-frame days after *B* maximum brightness (black). Line identification and colour codes are similar to those in Fig. 12.

**Table 3.** Nucleosynthetic yields and kinetic energies from the modelling using different density profiles compared to the original hydrodynamic models. Results from other SNe are also shown.

	$^{56}\text{Ni}$ $M_{\odot}$	$\text{Fe}^a$ $M_{\odot}$	$\text{Ni}_{\text{stable}}$ $M_{\odot}$	$\text{IME}^b$ $M_{\odot}$	O $M_{\odot}$	Total burned $M_{\odot}$	$E_k$ $10^{51}$ erg
1999aa (W7)	0.67	0.21	0.006	0.18	0.30	1.08	1.2
1999aa (DD2)	0.65	0.29	0.006	0.20	0.22	1.16	1.32
1999aa (DD3)	0.66	0.23	0.003	0.20	0.26	1.12	1.22
original W7	0.59	0.16	0.122	0.24	0.143	1.24	1.30
original DD2	0.69	0.10	0.054	0.33	0.066	1.31	1.40
original DD3	0.77	0.10	0.0664	0.25	0.056	1.32	1.43
1991T (DD3)	0.78	0.15	0.0006	0.18	0.29	1.09	1.24
2003du (W7)	0.62	0.18	0.024	0.26	0.23	1.15	1.25
2002bo (W7)	0.49	0.27	0.0001	0.28	0.11	1.27	1.24
2004eo (W7)	0.32	0.29	0.0005	0.43	0.3	1.1	1.1

Note. <sup>a</sup> All stable isotopes except for  $^{56}\text{Fe}$ , decay product of  $^{56}\text{Ni}$ .

<sup>b</sup>  $^{28}\text{Si} + ^{32}\text{S}$ .

against another observable. The light curve is one such observable. As is customary in our work, we computed synthetic bolometric light curves using the density and abundance distributions of the three models we tested. We used a Monte Carlo code that initially follows the emission and deposition of gamma rays and positrons, exactly as in the nebular spectrum calculations. The energy that is deposited is then assumed to be converted to optical photons, which are in turn transported through the ejecta using a time-dependent Monte Carlo scheme as outlined by Mazzali et al. (2001). The propagation of the optical photons is subject to an opacity. In the case of SNe Ia (and of all H-poor SNe), line opacity is the dominant opacity (Pauadrach et al. 1996). Line opacity can be parameterized based on the number of active lines in different species and the relative abundance of that species in the ejecta (Mazzali et al. 2001). Photon diffusion also depends on the mass in the ejecta and their expansion (i.e. their  $E_k$ ).

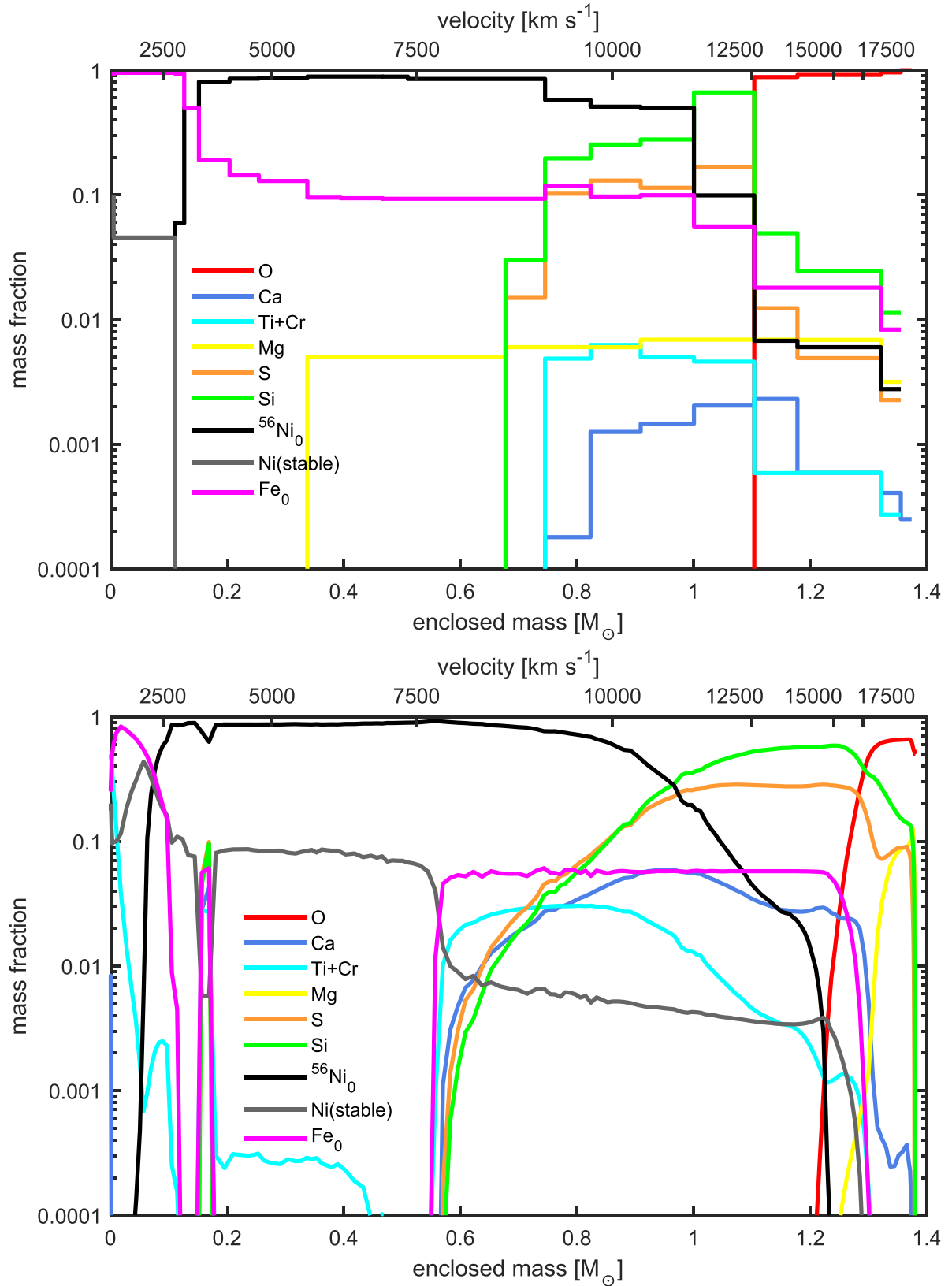


**Figure 14.** Upper panel: Abundances obtained from spectral models using the delayed detonation DD2 density profile. Lower panel: The original nucleosynthesis from DD2 (Iwamoto et al. 1999).



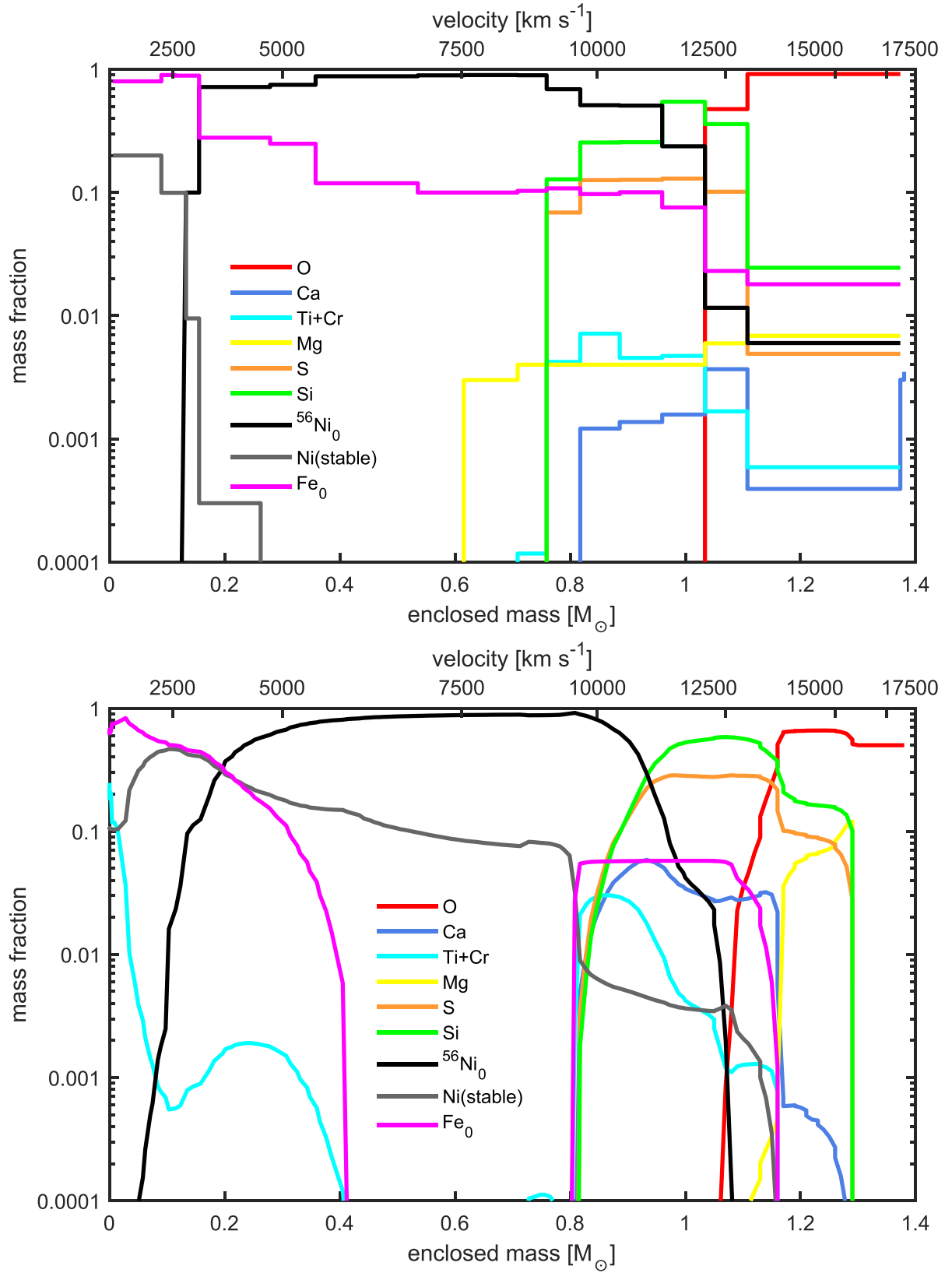


**Figure 15.** Upper panel: Abundances obtained from spectral models using the W7 density profile. Lower panel: The original nucleosynthesis from W7 (Nomoto et al. 1984).

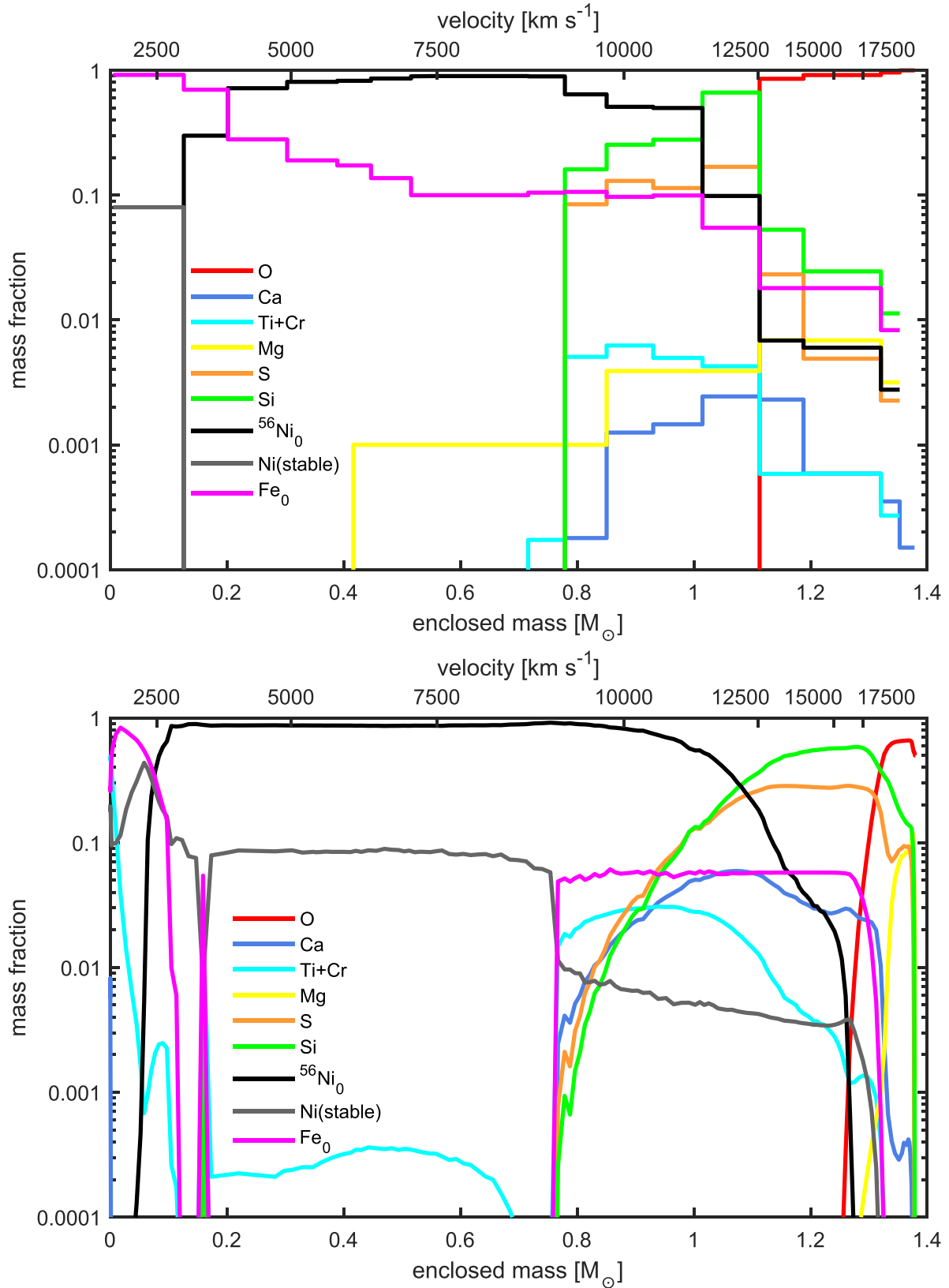


**Figure 16.** Upper panel: Abundances obtained from spectral models using the DD3 density profile. Lower panel: The original nucleosynthesis from DD3 (Iwamoto et al. 1999).

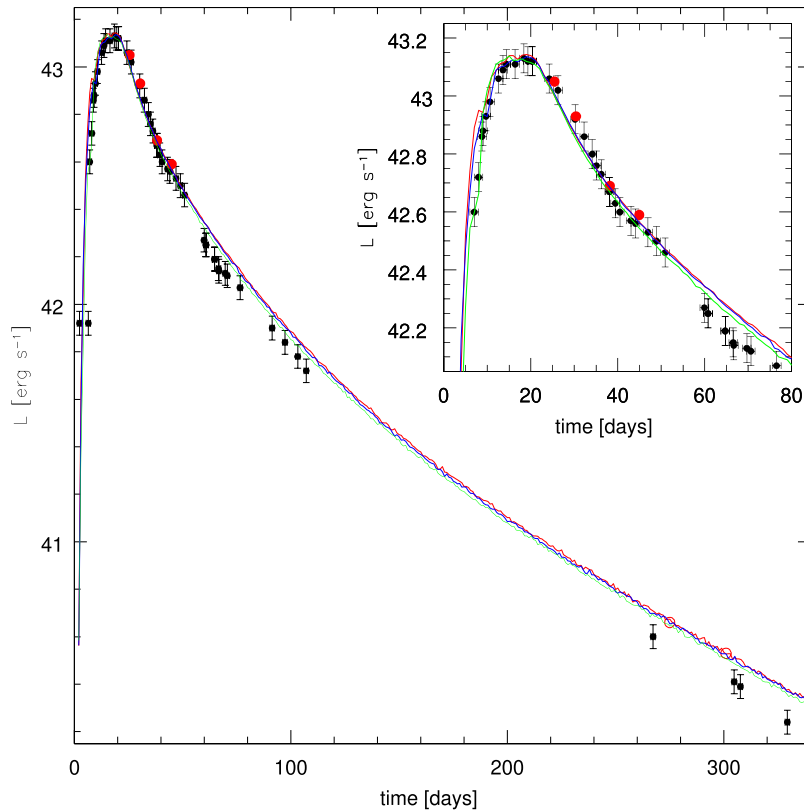


**Figure 17.** The *UBVRI* bolometric light curve of SN 1999aa (black dots), compared to the synthetic light curves computed using the density and abundance profiles of the three explosion models: W7 (red), DD2 (green), and DD3 (blue). Red points represent luminosities at the epochs when NIR observations are available from Krisciunas et al. (2000).

We computed synthetic bolometric light curves for our three explosion models. These are compared to the bolometric light curve of SN 1999aa in Fig. 17. All three synthetic light curves match the observed one reasonably well. While this suggests that the models we used and the abundances we derived are credible, it is difficult to choose a best-fitting model. Although DD2 yields the closest  $^{56}\text{Ni}$  mass to the value we obtained for SN 1999aa, the correspondence between the values we derived for the masses of the various elements and those in the original hydrodynamic calculation is not always perfect. Also, owing to the lack of early UV data, it is hard to constrain the densities in the outer layers. We can only conclude that DD2 is a reasonable model, but some modification is required. Most likely, a specific model would have to be derived for SN 1999aa, which may be similar to DD2 but may differ in some areas, as was the case for SN 2011fe (Mazzali et al. 2014, 2015).

## 8 DISCUSSION

Our synthetic spectra show reasonably good fits to the observed ones for the three density profiles used, with only small differences between them. For example, the Si II 6355 Å feature (Fig. 4), the O I 7744 Å line (Fig. 8), and the Fe II lines near 5000 Å (Fig. 10) are better reproduced with the DD2 and DD3 density profiles than with W7. However, these differences are marginal, and based on this criterion alone it is difficult to select a best-fitting model.

The yields of the most important elements or groups of elements are recapped in Table 3. From these yields we computed the expected

kinetic energy yield for each model using the formula

$$E_k = [1.56 M(^{56}\text{Ni}) + 1.47 M(\text{Fe}) + 1.24 M(\text{IME}) - E_{\text{bind}}] \times 10^{51} \text{ erg} \quad (1)$$

(Woosley et al. 2007), where  $E_{\text{bind}} = 0.46 \times 10^{51} \text{ erg}$  is the binding energy of the white dwarf. Results are given in Table 3. The values we obtain are slightly smaller than the original models. The difference may be explained by the weak burning at the outer shells. A similar behaviour was seen in SN 1991T (Sasdehli et al. 2014).

In Fig. 18, we compare the abundance distribution of SN 1999aa with those of three spectroscopically normal SNe Ia – SN 2003du [ $\Delta m_{15}(B) = 1.13 \text{ mag}$ , Tanaka et al. (2011)], SN 2002bo [ $\Delta m_{15}(B) = 1.13 \text{ mag}$ , Stehle et al. (2005)], and SN 2004eo [ $\Delta m_{15}(B) = 1.46 \text{ mag}$ , Mazzali et al. (2008)] – and with that of SN 1991T [ $\Delta m_{15}(B) = 0.94 \pm 0.05 \text{ mag}$ , Phillips et al. (1999)]. The plots show a striking similarity between the internal composition of SNe 1999aa and 1991T, but clear differences with respect to spectroscopically normal SNe Ia.

Most significantly, although IMEs reach a high abundance in a shell at  $\sim 11\,000 \text{ km s}^{-1}$ , the IME-dominated shell is very narrow, and therefore has little mass. At the outer edge, unlike in normal SNe Ia, the abundance of IMEs drops very sharply at  $v \approx 12\,000 \text{ km s}^{-1}$ , above which oxygen dominates.

This suggests that the weakness or absence of Si II and S II features in the earliest spectra of SN 1991T-like SNe Ia is not only an ionization effect but also the result of a low abundance (Mazzali et al. 1995). In these peculiar SNe, the IME abundance in the outermost

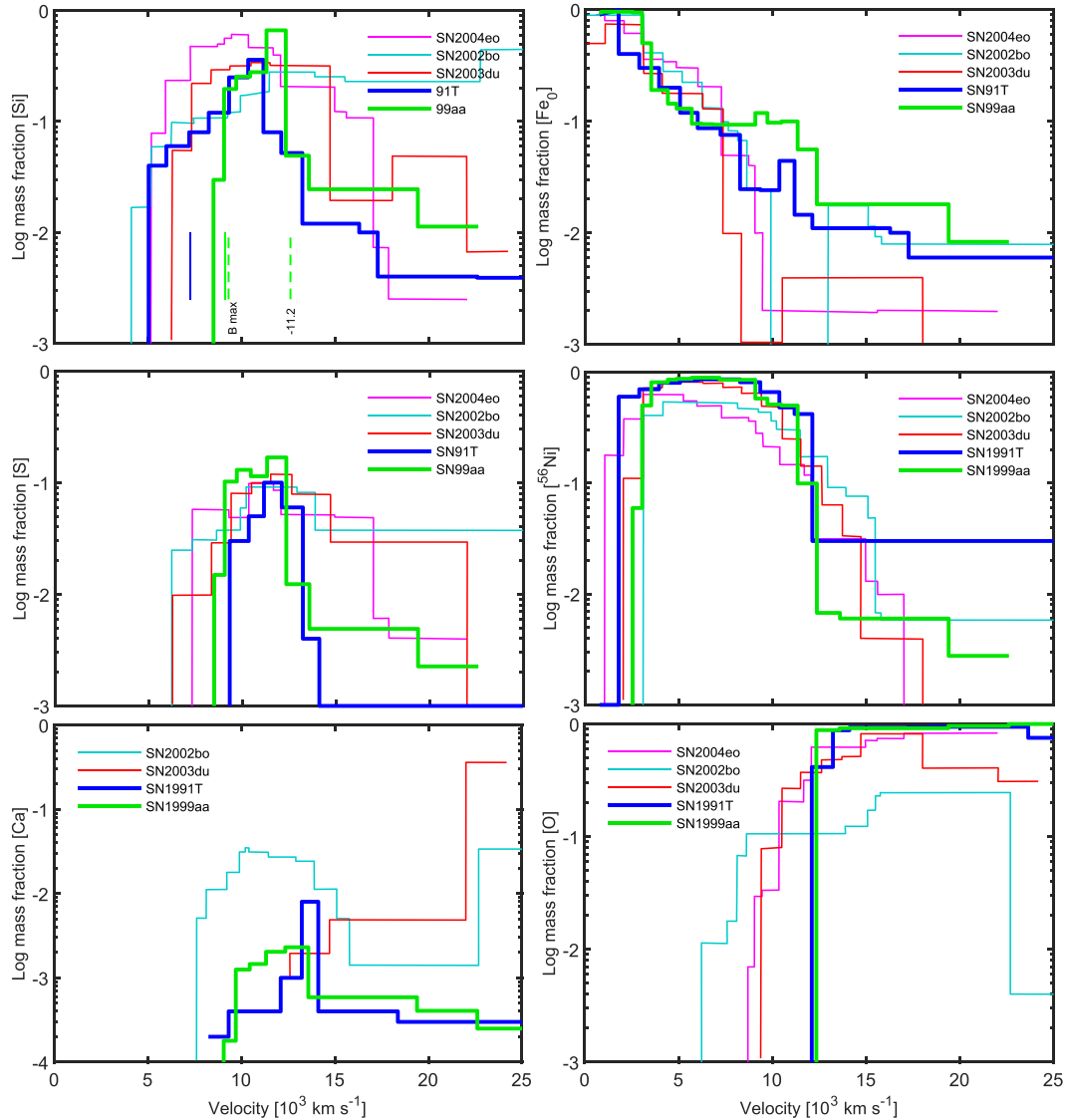


**Figure 18.** The distribution of the most important elements in SN 99aa, SN 1991T, and some spectroscopically normal SNe Ia. Left-hand side, top to bottom: Si, S, and Ca. Right-hand side, top to bottom: Stable Fe,  $^{56}\text{Ni}$ , and O. SNe 1999aa and 1991T have similar stratification properties: a more complete dominance of  $^{56}\text{Ni}$  in the inner layers (2000–10 000  $\text{km s}^{-1}$ ), a narrow IME shell peaking near 11 000  $\text{km s}^{-1}$  but terminating sharply above  $\sim 12$  000  $\text{km s}^{-1}$ , and a larger prevalence of oxygen in the outer layers, suggesting less burning in these regions. The dashed lines in the first panel show  $v_{\text{ph}}$  at days  $-11.2$  and at  $B$  maximum light. The continuous lines show the position of  $v_{\text{ph}}$  at the epochs when Fe II lines start to appear in SN 1999aa (green) and SN 1991T (blue).

layers is very small, and therefore the spectra start looking like those of normal SNe Ia at a later time.

In order to check the effect of the Si abundance on the spectra, we computed synthetic spectra using increasing quantities of Si at  $v \approx 12$  600  $\text{km s}^{-1}$ , at the expense of O, while keeping  $L_{\text{Bol}}$  and  $v_{\text{ph}}$  unchanged (Fig. 19). The Si II 6355 Å line in SN 1999aa is well reproduced with a Si abundance of  $\sim 0.025$ . As the Si abundance increases the line gets stronger, and it matches the spectrum of SN 2003du when the abundance is  $\sim 0.1$  at high velocities, which is comparable to the abundances reported in SN 2002bo (Stehle et al. 2005) and SN 2004eo (Mazzali et al. 2008). The abundance derived by Tanaka et al. (2011) for SN 2003du is even higher ( $\sim 0.3$  at  $v \approx 10$  500–15 000  $\text{km s}^{-1}$ ).

Although the spectroscopic properties of SN 1999aa suggest that it is physically intermediate between SN 1991T and normal

SNe Ia, its photometric properties do not. Our modelling shows that the amount of  $^{56}\text{Ni}$  synthesized in SN 1999aa ( $\sim 0.65 M_{\odot}$ ) is less than in SN 1991T ( $\sim 0.78 M_{\odot}$ , Sasdelli et al. 2014), suggesting that SN 1999aa should be less luminous than SN 1991T (see Fig. 20). However, SN 1999aa was a slower decliner than SN 1991T. SN 1999aa has estimated  $\Delta m_{15}(B)$  values ranging from 0.75 mag (Krisciunas et al. 2000) to 0.85 mag (Jha et al. 2006), which may be taken to imply that it was actually more luminous than SN 1991T [ $\Delta m_{15}(B) = 0.94$  mag].

However, a comparison of the bolometric light curves of the two SNe shows that relying on a  $\Delta m_{15}(B)$  alone would be misleading. The light curve of SN 1991T is brighter throughout, as it should be based on the  $^{56}\text{Ni}$  mass. However, it peaks much earlier than that of SN 1999aa. This is because the  $^{56}\text{Ni}$  abundance in the outer layers of SN 1991T is larger than in SN 1999aa, causing a faster rise to



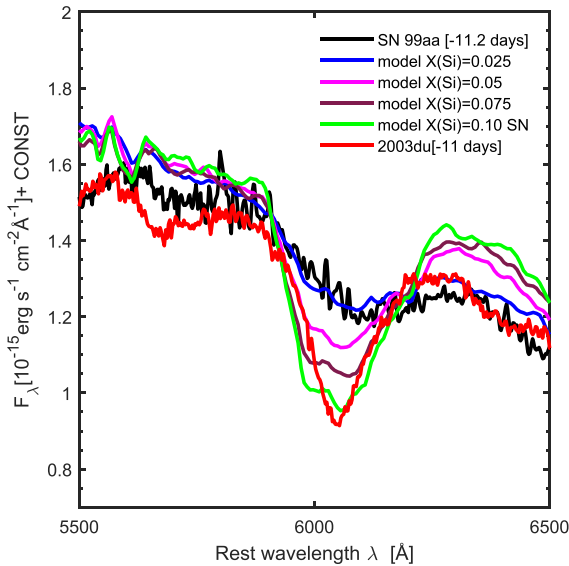


**Figure 19.** The effect of changing the Si abundance in the outermost layers.

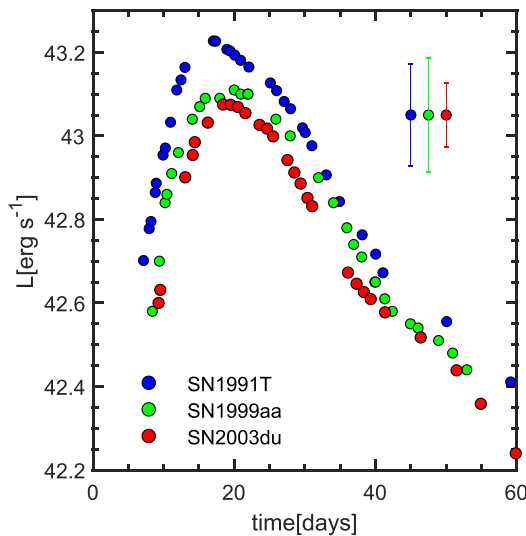


**Figure 20.** The bolometric light curve of SN 1999aa (green) compared to those of SN 1991T (Sasdehli et al. 2014, blue) and SN 2003du (Stanishev et al. 2007, red). The UV contribution was removed from the light curve of SN 2003du to allow a proper comparison, as no UV information is available for the other two SNe. Error bars for SN 1999aa and SN 1991T represent statistical errors due to distance moduli uncertainties  $\delta\mu$ , to the host galaxies using the Tully–Fisher relation:  $\delta\mu[99aa] = 0.34$  and  $\delta\mu[91T] = 0.30$ . The error bar for SN 2003du is calculated taking  $\delta\mu[03du] = 0.19$  (Stanishev et al. 2007).

a very luminous maximum (see Fig. 18). The luminous phase is then sustained by the larger  $^{56}\text{Ni}$  mass, but the contrast between the nominal luminosity at peak and that 15 d later is larger than in SN 1999aa, which reaches maximum brightness later. This may mean that  $\Delta m_{15}(B)$  is not valid for the SN 1991T class (see also Pinto & Eastman 2000; Woosley et al. 2007; Scalzo et al. 2012), and it was also suggested for objects at the faint end of the luminosity–width relation (Ashall et al. 2018). On the other hand, SN 2003du and SN 1999aa, reach peak luminosities that differ by only  $\log(L) \lesssim 0.05$ , even though they have different decline rates and different

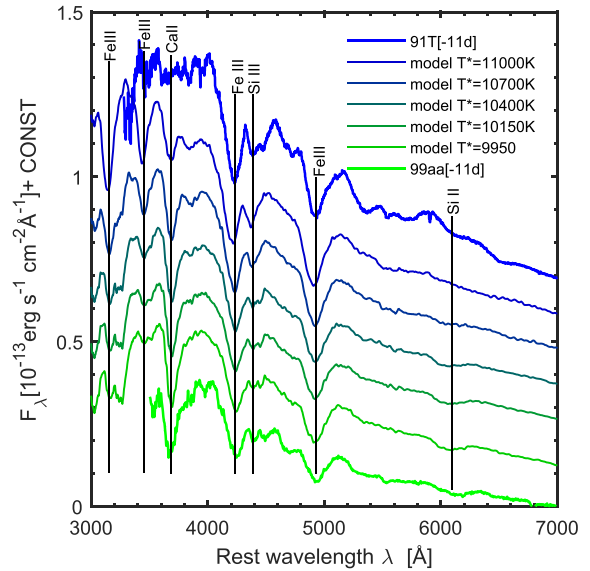


**Figure 21.** Early-time spectra of SNe 1999aa and 1991T compared to synthetic spectra computed for increasing luminosity but the same composition. As the luminosity increases the spectra morph from looking like SN 1999aa to looking like SN 1991T.

spectroscopic properties. Despite the distance uncertainties, this result can be taken to confirm that both of these events synthesize a similar mass of  $^{56}\text{Ni}$  as suggested from our spectral modelling (approximately  $0.62\text{--}0.65 M_{\odot}$ , see Table 3).

Even though the abundance distributions in SNe 1999aa and 1991T are similar, their spectroscopic evolution shows differences. These can be explained by the difference in luminosity between the two SNe. We computed synthetic spectra at day  $-11$  starting from the model that matches SN 1999aa and progressively increased the luminosity (Fig. 21). As the luminosity increases, the spectrum changes, until it finally starts resembling that of SN 1991T: The Si II 6355 Å line becomes weaker, and so does Ca II H&K. The same is true for the Fe III features observed near 3200, 3500, 4200, and 4900 Å.

SNe Ia exhibit very similar spectroscopic properties beyond maximum brightness. Therefore, an explosion-progenitor scenario that can explain the complete spectroscopic sequence should be one that allows variations only in the outer layers. The sudden depletion of the IMEs in the outer shells of SN 1999aa is not easy to explain within the framework of conventional delayed-detonation explosion models (Khokhlov 1991b; Iwamoto et al. 1999). One possible explanation may be an explosion that initially proceeds very efficiently but then suddenly stops, leaving an only weakly burned outer layer. One such class of models is pulsation-driven detonations (Ivanova, Imshennik & Chechetkin 1974; Khokhlov 1991a; Hoefflich, Khokhlov & Wheeler 1995). In these configurations, the progenitor is characterized by an outer layer with low density, which could be the result of the pre-expansion of a white dwarf that has gone through an initial failed burning phase, or to a binary merger. This results in a steep density gradient and may cause IMEs to be confined in a relatively narrow velocity range. However, these models predict no burning in the outermost layers, and therefore the presence of a copious amount of C (Baron et al. 2008), which is not observed in SN 1999aa or SN 1991T. Additionally, simulations of these models show IME lines at very early times, and do not resemble the spectra of SN 1991T-like SNe Ia (Dessart et al. 2014). Furthermore,

three-dimensional versions of these models exhibit a large degree of mixing and cannot explain the stratification seen in SN 1999aa (Plewa, Calder & Lamb 2004; Kasen & Plewa 2005; Bravo & García-Senz 2009; Bravo et al. 2009).

In general, none of the currently available models can explain the entire spectroscopic properties of SNe Ia over a large range of luminosities. Nevertheless, the pulsation-driven scenario remains interesting for SN 1991T-like SNe because it only affects the outer ejecta. Based on our current knowledge, this particular scenario should only kick in when  $^{56}\text{Ni}$  production is very high.

## 9 CONCLUSIONS

We have modelled a series of optical spectra of the peculiar slow decliner SN 1999aa, from  $-12$  to  $+300$  d from  $B$  maximum to infer the composition layering of its ejecta. Three different density profiles were used – the fast deflagration W7 and two delayed detonation models, DD2 and DD3. We have compared our results with spectroscopically normal events as well as with SN 1991T.

Our main results can be summarized as follows.

(i) All three density profiles yield synthetic spectra similar to the observed ones and follow their evolution. In particular, an Fe III-dominated early-time spectrum with shallow IME lines, typical of the SN 1991T class, is reproduced.

(ii) The internal composition of SN 1999aa is dominated by neutron-rich iron-peak elements, as in normal SNe Ia. This is followed by a  $^{56}\text{Ni}$  shell (mass  $\approx 0.65 M_{\odot}$ ). Above this lies a narrow IME shell which is sharply separated from the outer, O-dominated shell.

(iii) The confinement of IMEs to a narrow velocity range and their depletion in the outermost layers indicates a sudden shift from a regime of strong burning to one of weak incomplete burning. This behaviour is remarkably similar to that of SN 1991T, but is not observed in normal SNe Ia. Therefore, it is reasonable to conclude that SN 1999aa and 1991T share a similar explosion mechanism, despite their somewhat different luminosities.

(iv) The observed stratification may be the result of sharp density gradients in the outer shells of the progenitor.

(v) The spectroscopic path from normal SNe Ia to the brightest peculiar events cannot be explained solely by a luminosity/temperature sequence. It should involve composition layering differences suggesting variations either in the density structure of the progenitor white dwarf at the outer layers or in details of the explosion.

(vi) Within the SN 1991T class, IME confinement coupled with differences in luminosity (i.e.  $^{56}\text{Ni}$  production) may explain the observed spectra.

## ACKNOWLEDGEMENTS

This work has used data collected at the Italian *Telescopio Nazionale Galileo (TNG)*, which is operated on the island of La Palma by the Fundacion Galileo Galilei of the INAF (Istituto Nazionale di Astrofisica) at the Spanish Observatorio del Roque de los Muchachos of the Instituto de Astrofisica de Canarias. The authors thank the anonymous referee for his well thought comments that improved the quality of this study. C.A. thanks Roger Hajjar and Sami Dib for discussions, and Amy Sidaoui for English review.

A.V.F. is grateful for financial support provided by the U.S. National Science Foundation, the Christopher R. Redlich Fund, and many individual donors. This research has made use of the NASA/IPAC Extragalactic Database (NED) which is operated by the

Jet Propulsion Laboratory, California Institute of Technology, under contract with the National Aeronautics and Space Administration.

Some of the data presented herein were obtained at the W. M. Keck Observatory, which is operated as a scientific partnership among the California Institute of Technology, the University of California, and NASA; the observatory was made possible by the generous financial support of the W. M. Keck Foundation. The Kast spectrograph on the Shane 3 m telescope at Lick Observatory was made possible through a gift from William and Marina Kast. Research at Lick Observatory is partially supported by a generous gift from Google. We thank the staffs at the various observatories where data were obtained.

## DATA AVAILABILITY

The spectroscopic data used in this article are available at the Weizmann Interactive Supernova Data Repository (WiSeREP, Yaron & Gal-Yam 2012).

## REFERENCES

- Altavilla G. et al., 2004, *MNRAS*, 349, 1344  
 Amanullah R. et al., 2010, *ApJ*, 716, 712  
 Armstrong M., Schwartz M., 1999, *Int. Astron. Union Circ.*, 7108, 1  
 Arnett W. D., 1982, *ApJ*, 253, 785  
 Ashall C., Mazzali P. A., Pian E., James P. A., 2016, *MNRAS*, 463, 1891  
 Ashall C. et al., 2018, *MNRAS*, 477, 153  
 Asplund M., Grevesse N., Sauval A. J., Scott P., 2009, *ARA&A*, 47, 481  
 Axelrod T. S., 1980, in Wheeler J. C., ed., *Proc. Texas Workshop on Type I Supernovae, Late Time Optical Spectra from the Ni-56 Model for Type I Supernovae*. Univ. Texas, Texas, p. 80  
 Ayani K., Yamaoka H., 1998, *Int. Astron. Union Circ.*, 7059, 1  
 Baron E., Jeffery D. J., Branch D., Bravo E., García-Senz D., Hauschildt P. H., 2008, *ApJ*, 672, 1038  
 Bottinelli L., Gouguenheim L., Paturel G., de Vaucouleurs G., 1985, *A&AS*, 59, 43  
 Branch D., 2001, *PASP*, 113, 169  
 Bravo E., García-Senz D., 2009, *ApJ*, 695, 1244  
 Bravo E., García-Senz D., Cabezón R. M., Domínguez I., 2009, *ApJ*, 695, 1257  
 Cappellaro E., 2014, *Snoopy: A Package for SN Photometry*. <http://sngroup.oapd.inaf.it/snoopy.html>  
 Cappellaro E., Mazzali P. A., Benetti S., Danziger I. J., Turatto M., della Valle M., Patat F., 1997, *A&A*, 328, 203  
 Cardelli J. A., Clayton G. C., Mathis J. S., 1989, *ApJ*, 345, 245  
 Chonis T. S., Gaskell C. M., 2008, *AJ*, 135, 264  
 Dessart L., Blondin S., Hillier D. J., Khokhlov A., 2014, *MNRAS*, 441, 532  
 Epinat B. et al., 2008, *MNRAS*, 388, 500  
 Filippenko A. V., 1997, *ARA&A*, 35, 309  
 Filippenko A. V. et al., 1992, *ApJ*, 384, L15  
 Fukugita M., Shimasaku K., Ichikawa T., 1995, *PASP*, 107, 945  
 Galbany L. et al., 2016, *A&A*, 591, A48  
 Garavini G. et al., 2004, *AJ*, 128, 387  
 Graham M. L., Nugent P. E., Sullivan M., Filippenko A. V., Cenko S. B., Silverman J. M., Clubb K. I., Zheng W., 2015, *MNRAS*, 454, 1948  
 Hachinger S. et al., 2013, *MNRAS*, 429, 2228  
 Hachisu I., Kato M., Saio H., Nomoto K., 2012, *ApJ*, 744, 69  
 Hillebrandt W., Niemeyer J. C., 2000, *ARA&A*, 38, 191  
 Hoeflich P., Khokhlov A. M., Wheeler J. C., 1995, *ApJ*, 444, 831  
 Ivanova L. N., Imshennik V. S., Chechetkin V. M., 1974, *Ap&SS*, 31, 497  
 Iwamoto K., Brachwitz F., Nomoto K., Kishimoto N., Umeda H., Hix W. R., Thielemann F.-K., 1999, *ApJS*, 125, 439  
 Jeffery D. J., Leibundgut B., Kirshner R. P., Benetti S., Branch D., Sonneborn G., 1992, *ApJ*, 397, 304  
 Jha S. et al., 2006, *AJ*, 131, 527  
 Jha S. W., Maguire K., Sullivan M., 2019, *Nature Astron.*, 3, 706  
 Justham S., 2011, *ApJ*, 730, L34

- Kasen D., Plewa T., 2005, *ApJ*, 622, L41
- Khokhlov A. M., 1991a, *A&A*, 245, L25
- Khokhlov A. M., 1991b, *A&A*, 245, 114
- Krisciunas K., Hastings N. C., Loomis K., McMillan R., Rest A., Riess A. G., Stubbs C., 2000, *ApJ*, 539, 658
- Kuchner M. J., Kirshner R. P., Pinto P. A., Leibundgut B., 1994, *ApJ*, 426, L89
- Livio M., Mazzali P., 2018, *Phys. Rep.*, 736, 1
- Lucy L. B., 1999a, *A&A*, 344, 282
- Lucy L. B., 1999b, *A&A*, 345, 211
- Marietta E., Burrows A., Fryxell B., 2000, *ApJS*, 128, 615
- Marion G. H., Höflich P., Wheeler J. C., Robinson E. L., Gerardy C. L., Vacca W. D., 2006, *ApJ*, 645, 1392
- Matheson T. et al., 2008, *AJ*, 135, 1598
- Mazzali P. A., 2000, *A&A*, 363, 705
- Mazzali P. A., 2001, *MNRAS*, 321, 341
- Mazzali P. A., Lucy L. B., 1993, *A&A*, 279, 447
- Mazzali P. A., Lucy L. B., Danziger I. J., Gouiffes C., Cappellaro E., Turatto M., 1993, *A&A*, 269, 423
- Mazzali P. A., Danziger I. J., Turatto M., 1995, *A&A*, 297, 509
- Mazzali P. A., Chugai N., Turatto M., Lucy L. B., Danziger I. J., Cappellaro E., della Valle M., Benetti S., 1997, *MNRAS*, 284, 151
- Mazzali P. A., Cappellaro E., Danziger I. J., Turatto M., Benetti S., 1998, *ApJ*, 499, L49
- Mazzali P. A., Nomoto K., Cappellaro E., Nakamura T., Umeda H., Iwamoto K., 2001, *ApJ*, 547, 988
- Mazzali P. A., Benetti S., Stehle M., Branch D., Deng J., Maeda K., Nomoto K., Hamuy M., 2005a, *MNRAS*, 357, 200
- Mazzali P. A. et al., 2005b, *ApJ*, 623, L37
- Mazzali P. A., Röpke F. K., Benetti S., Hillebrandt W., 2007, *Science*, 315, 825
- Mazzali P. A., Sauer D. N., Pastorello A., Benetti S., Hillebrandt W., 2008, *MNRAS*, 386, 1897
- Mazzali P. A. et al., 2014, *MNRAS*, 439, 1959
- Mazzali P. A. et al., 2015, *MNRAS*, 450, 2631
- Mazzali P. A. et al., 2020, *MNRAS*, 494, 2809
- Nakano S., Kushida R., Kushida Y., 1999, *Int. Astron. Union Circ.*, 7109, 4
- Nomoto K., Thielemann F. K., Yokoi K., 1984, *ApJ*, 286, 644
- Oke J. B. et al., 1995, *PASP*, 107, 375
- Panagia N., Van Dyk S. D., Weiler K. W., Sramek R. A., Stockdale C. J., Murata K. P., 2006, *ApJ*, 646, 369
- Parrent J. T. et al., 2011, *ApJ*, 732, 30
- Parrent J., Friesen B., Parthasarathy M., 2014, *Ap&SS*, 351, 1
- Pauldrach A. W. A., Duschinger M., Mazzali P. A., Puls J., Lennon M., Miller D. L., 1996, *A&A*, 312, 525
- Perlmutter S. et al., 1998, *Nature*, 391, 51
- Phillips M. M., 1993, *ApJ*, 413, L105
- Phillips M. M., Lira P., Suntzeff N. B., Schommer R. A., Hamuy M., Maza J., 1999, *AJ*, 118, 1766
- Pinto P. A., Eastman R. G., 2000, *ApJ*, 530, 744
- Plewa T., Calder A. C., Lamb D. Q., 2004, *ApJ*, 612, L37
- Qiao Q. Y., Wei J. Y., Qiu Y. L., Hu J. Y., 1999, *Int. Astron. Union Circ.*, 7109, 3
- Riess A. G. et al., 1998, *AJ*, 116, 1009
- Riess A. G. et al., 2004, *ApJ*, 607, 665
- Saselli M., Mazzali P. A., Pian E., Nomoto K., Hachinger S., Cappellaro E., Benetti S., 2014, *MNRAS*, 445, 711
- Scalzo R. et al., 2012, *ApJ*, 757, 12
- Schlegel D. J., Finkbeiner D. P., Davis M., 1998, *ApJ*, 500, 525
- Siebert M. R. et al., 2019, *MNRAS*, 486, 5785
- Silverman J. M. et al., 2012a, *MNRAS*, 425, 1789
- Silverman J. M., Kong J. J., Filippenko A. V., 2012b, *MNRAS*, 425, 1819
- Silverman J. M. et al., 2012c, *ApJ*, 756, L7
- Silverman J. M., Vinkó J., Marion G. H., Wheeler J. C., Barna B., Szalai T., Mulligan B. W., Filippenko A. V., 2015, *MNRAS*, 451, 1973
- Stanishev V. et al., 2007, *A&A*, 469, 645
- Stehle M., Mazzali P. A., Benetti S., Hillebrandt W., 2005, *MNRAS*, 360, 1231
- Tanaka M. et al., 2008, *ApJ*, 677, 448
- Tanaka M., Mazzali P. A., Stanishev V., Maurer I., Kerzendorf W. E., Nomoto K., 2011, *MNRAS*, 410, 1725
- Theureau G., Hanski M. O., Coudreau N., Hallet N., Martin J. M., 2007, *A&A*, 465, 71
- van Driel W. et al., 2016, *A&A*, 595, A118
- Woosley S. E., 2007, *ApJ*, 668, 1109
- Woosley S. E., Kasen D., Blinnikov S., Sorokina E., 2007, *ApJ*, 662, 487
- Yaron O., Gal-Yam A., 2012, *PASP*, 124, 668
- Yoshida S., Kadota K., Kiss L., Csak B., Moretti S., Tomaselli S., 1999, *Int. Astron. Union Circ.*, 7139, 3

This paper has been typeset from a  $\text{\LaTeX}$  file prepared by the author.